Homocysteine fibrillar assemblies display cross-talk with Alzheimer's disease β-amyloid polypeptide

Dorin Sade Yazdi[a], Dana Laor Bar-Yosef[a], Hanaa Adsi[a], Topaz Kreiser[a], Shahaf Sigal[b,c], Santu Bera[a], Dor Zaguri[a], Shira Shaham-Niv[d], Damilola S. Oluwatoba[e], Davide Levy[f], Myra Gartner[a], Thanh D. Do[e], Dan Frenkel[b,c], and Ehud Gazit[a,c,d,1]

[a]The Shmunis School of Biomedicine and Cancer Research, Tel Aviv University, 6997801 Tel Aviv, Israel; [b]Department of Neurobiology, George S. Wise Faculty of Life Sciences, The School of Neurobiology, Biochemistry and Biophysics, Tel Aviv University, 6997801 Tel Aviv, Israel; [c]Sagol Interdisciplinary School of Neurosciences, Tel Aviv University, 6997801 Tel Aviv, Israel; [d]Blavatnik Center for Drug Discovery, Tel Aviv University, 6997801 Tel Aviv, Israel; [e]Department of Chemistry, University of Tennessee, Knoxville, TN 37996; and [f]Wolfson Applied Materials Research Center, Tel Aviv University, 6997801 Tel Aviv, Israel

Edited by Michele Vendruscolo, University of Cambridge, Cambridge, United Kingdom, and accepted by Editorial Board Member F. Ulrich Hartl April 18, 2021 (received for review August 19, 2020)

High levels of homocysteine are reported as a risk factor for Alzheimer's disease (AD). Correspondingly, inborn hyperhomocysteinemia is associated with an increased predisposition to the development of dementia in later stages of life. Yet, the mechanistic link between homocysteine accumulation and the pathological neurodegenerative processes is still elusive. Furthermore, despite the clear association between protein aggregation and AD, attempts to develop therapy that specifically targets this process have not been successful. It is envisioned that the failure in the development of efficacious therapeutic intervention may lie in the metabolomic state of affected individuals. We recently demonstrated the ability of metabolites to self-assemble and cross-seed the aggregation of pathological proteins, suggesting a role for metabolite structures in the initiation of neurodegenerative diseases. Here, we provide a report of homocysteine crystal structure and self-assembly into amyloid-like toxic fibrils, their inhibition by polyphenols, and their ability to seed the aggregation of the AD-associated β-amyloid polypeptide. A yeast model of hyperhomocysteinemia indicates a toxic effect, correlated with increased intracellular amyloid staining that could be rescued by polyphenol treatment. Analysis of AD mouse model brain sections indicates the presence of homocysteine assemblies and the interplay between β-amyloid and homocysteine. This work implies a molecular basis for the association between homocysteine accumulation and AD pathology, potentially leading to a paradigm shift in the understanding of AD initial pathological processes.

Alzheimer's disease | metabolite amyloids | cross-seeding | homocysteine | hyperhomocysteinemia

Alzheimer's disease (AD) is the most common neurodegenerative disorder, currently affecting tens of millions of individuals globally and leading to immense social and financial impacts (1, 2). Despite the vast efforts to develop a pharmacological treatment for the disease, recent clinical trials had failed (3, 4). While it is very clear that amyloid formation is associated with AD (5, 6) and genetic variations in the gene coding for the β-amyloid polypeptide are associated with early onset of the disease (7), direct targeting of the aggregation of AD-associated pathological proteins and polypeptides has so far not resulted in clinical development of any disease-modifying treatment (8–10). Therefore, there is an essential need to understand the early biological changes that may induce the diverse pathologies observed in AD and other forms of dementia in order to identify new therapeutic targets (10).

In the last decades, an enormous body of research had provided important information on the amyloid cascade, oxidative stress, and inflammatory response that are involved in AD (3, 11). Specifically, the notion of β-amyloid toxicity and extracellular plaque formation as the main cause of neuronal and synaptic loss has been extensively studied (12–14). Yet, the key to AD treatment and prevention remains elusive, and the initial steps leading to the formation and accumulation of these protein aggregates and the role of nonproteinaceous agents in this process are still not understood (10). Since only 1% of AD cases result from a familial mutation and the majority of patients are sporadic (2, 4), it is important to explore new directions to understand the biological mechanisms underlying these cases. Studies of metabolite profiling in brain regions and body fluids of AD and Parkinson's disease (PD) patients show interference with specific metabolic pathways (15–19). Homocysteine (Hcy), a noncoded amino acid, was identified as a major risk factor for AD as high plasma concentrations were associated with the progression of the disease (20–22). Higher Hcy serum concentration was also correlated with behavioral and psychological symptoms of AD (23) and was associated with changes in motor function and cognitive decline in PD as well as with a more severe cognitive impairment in elderly adults (24–26). Furthermore, it was shown that significantly decreased hippocampal and cortical volume is associated with increased Hcy plasma concentration (27).

Cystathionine β-synthase (CBS) deficiency, leading to excess of Hcy, results in the hyperhomocysteinemia inborn error of metabolism (IEM) disorder characterized by severe cognitive consequences (28–30). While elevated plasma Hcy is frequently reported as a strong and independent risk factor for the development of cognitive decline and dementia, the mechanism of its involvement is elusive (20, 31–34). Interestingly, the association between Hcy

Significance

The accumulation of homocysteine, a key metabolite, is considered a risk factor for Alzheimer's disease. This work demonstrates the ability of homocysteine to form ordered fibrillar structures. The toxicity of these structures is demonstrated in a yeast model that accumulates homocysteine. We further show the association of this observation with Alzheimer's disease pathology, including induced aggregation of a pathological protein and the presence of homocysteine structures in the brain of model mice. We suggest the targeting of homocysteine structure formation as a direction for Alzheimer's disease therapeutics.

Author contributions: D.S.Y., D.L.B.-Y., S.S., S.B., S.S.-N., T.D.D., D.F., and E.G. designed research; D.S.Y., D.L.B.-Y., H.A., T.K., S.S., S.B., D.Z., D.S.O., D.L., M.G., and T.D.D. performed research; D.S.Y., D.L.B.-Y., S.S., S.B., S.S.-N., T.D.D., and D.F. analyzed data; and D.S.Y., D.L.B.-Y., and E.G. wrote the paper.

The authors declare no competing interest.

This article is a PNAS Direct Submission. M.V. is a guest editor invited by the Editorial Board.

[1]To whom correspondence may be addressed. Email: ehudga@tauex.tau.ac.il.

This article contains supporting information online at https://www.pnas.org/lookup/suppl/doi:10.1073/pnas.2017575118/-/DCSupplemental.

Published June 7, 2021.

and AD-related pathological proteins was also demonstrated. Hcy-rich medium was shown to be cytotoxic to hippocampal and cortical neurons, resulting in increased β-amyloid–induced cell death (35–37). In addition, Hcy was found to bind β-amyloid$_{1\text{-}40}$, thereby stimulating β-sheet structure formation to facilitate its deposition. Indeed, induced Hcy accumulation in the brains of rats caused an elevation of β-amyloid deposition (38, 39). Furthermore, Hcy increased total tau and phosphorylated tau protein levels as well as the level of tau oligomers (40). Although the involvement of Hcy accumulation in AD pathology is evidential, no mechanistic insight has so far been suggested.

We have previously demonstrated that small metabolites can self-assemble into amyloid-like structures with amyloidogenic characteristics (41–44). The presence of metabolite assemblies in IEM disorders (e.g., phenylalanine in Phenylketonuria) exemplifies their physiological importance in pathologically diversified diseases. Interestingly, recent studies demonstrated that metabolite assemblies could cross-seed the aggregation of proteins under physiological conditions, thereby suggesting a possible mechanism in which accumulated metabolites interfere with protein function and folding (45, 46). Assemblies of quinolinic acid, an endogenous neurometabolite that is involved in the pathology of PD, induce the aggregation of α-synuclein both in vitro and in cell culture (45). In addition, phenylalanine preformed fibrils were shown to initiate the aggregation of several proteins under physiological conditions (46). Metabolite accumulation, structure formation, and seeding of proteins may thus underlie the unknown role of metabolites in neurodegenerative pathologies (47). Specifically, seeding of amyloidogenic proteins by preformed fibrils may be part of the mechanisms underlying the stereotypical spreading of toxic aggregates in the brains of AD patients.

We recently established an in vivo yeast model for IEM disorders by genetically modifying the yeast to reflect the mutations found in patients showing accumulation of the adenine nucleobase and its derivatives (48). Yeast model systems provide a powerful platform to elucidate the pathophysiology of diseases, as well as for the screening and development of disease-modifying therapeutics (49). This model was found to be a valid system, as supported by its robust sensitivity to adenine feeding and by the fact that adenine supramolecular structures could be detected. Furthermore, the

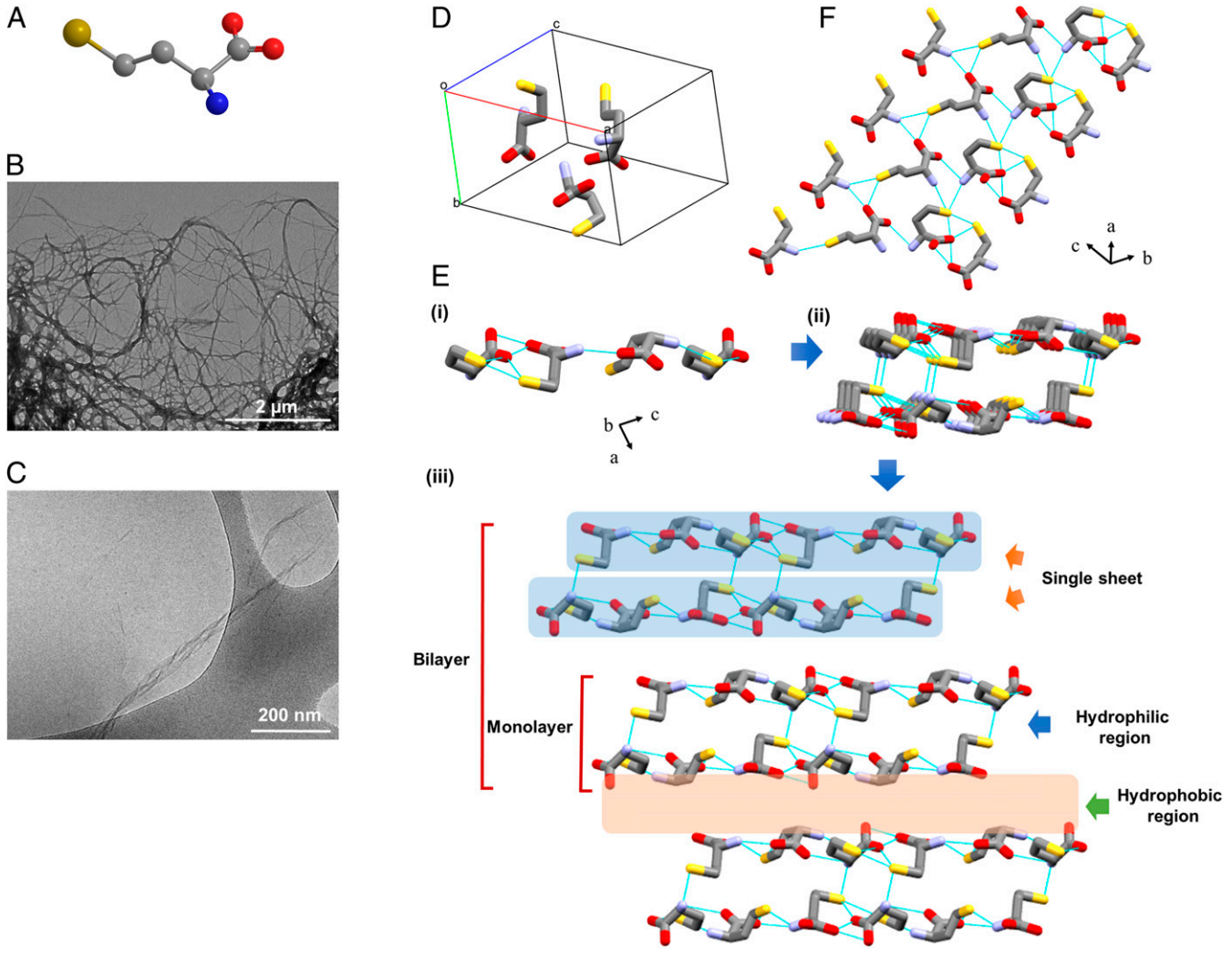

Fig. 1. Characterization of Hcy assemblies. (*A*) Skeletal formula of Hcy in a ball and stick model. The carbon atoms are represented in gray, and nitrogen, oxygen, and sulfur heteroatoms are shown in blue, red, and yellow, respectively. Hydrogen atoms are omitted for clarity. (*B*) TEM and (*C*) cryo-TEM micrographs of preformed samples of Hcy assemblies (2 mg/mL). (*D–F*) Single-crystal structure of Hcy. (*D*) The solid-state conformation in the asymmetric unit. (*E*) *i*) Side view of the H-bonded single sheet in the *b*-direction. *ii)* Formation of a single layer by two adjacent sheets through intermolecular H-bonding. *iii)* Layer-by-layer structure formation by hydrophobic interactions resembles supramolecular β-sheet structure. The hydrophobic and hydrophilic regions are indicated by arrows. (*F*) Top view of the single sheet. Hydrogen bonds are shown as light blue lines.

addition of a generic fibrillation-modifying polyphenolic compound rescued the toxic effect without lowering the concentration of adenine, indicating the therapeutic potential of our model for the modulation of structure formation (48, 50).

Here, aiming to explore the role of Hcy in AD, we demonstrate the formation of amyloid-like fibrils by Hcy in vitro and in vivo in a yeast model. Structural characterization of the Hcy fibrils and their cytotoxic effect were both studied. In addition, we revealed that polyphenolic inhibitors could rescue the toxic effect of Hcy assemblies and inhibit its structure formation. Remarkably, immunohistochemistry allowed the detection of Hcy fibrils in the brain of AD model mice as well as the apparent interplay between Hcy and β-amyloid. Finally, we demonstrated the cross-seeding of AD-related pathological protein by Hcy assemblies. Our work suggests a research direction for the association between metabolite accumulation and the initiation of neurodegenerative processes, thus offering a path for the development of therapeutic treatments that will target the key early stages of the disease.

Results

Self-Assembly of Hcy to Form Amyloid-like Fibrils and Their Structural Analysis. We first examined whether Hcy, a sulfur-containing noncoded amino acid (Fig. 1*A*), can self-assemble into ordered supramolecular structures. To examine the possible in vitro self-association of Hcy and to further characterize the assemblies, we dissolved Hcy to obtain a homogenous solution, which resulted in its self-assembly into ordered fibrillary structures. As assessed by transmission electron microscopy (TEM), Hcy formed amyloid-like fibrils that could be detected by structure adsorption to a copper grid (Fig. 1*B*) as well as in the solution, as demonstrated using cryogenic TEM (cryo-TEM) (Fig. 1*C*). Hcy fibrils could be detected at various concentrations (*SI Appendix*, Fig. S1).

Despite its vast biological importance, the crystal structure of Hcy has not been reported in the literature. To determine the molecular arrangement of Hcy at the atomic level and the overall packing, we set out to solve the single-crystal structure of Hcy. Due to the challenge of growing single crystals of sufficient size and quality for single-crystal diffraction, powder X-ray diffraction (PXRD) methods were employed to determine the crystal structure of Hcy, as previously used for the crystal structure determination of L-Lysine (51). The freeze-dried samples of self-assembled Hcy typically give rise to a microcrystalline powder of the anhydrous phase, thus requiring PXRD for structure determination. The solved structure from the PXRD pattern contained three molecules of Hcy in the unit cell with triclinic P-1 space group comprising a = 10.27 Å, b = 7.01 Å, c = 14.15 Å, α = 99.08°, β = 75.75°, and γ = 68.31° (Fig. 1*D*). The crystal structure of Hcy can be described as a layered arrangement (a supramolecular β-sheet), similar to the crystal structures of various single amino acids (52, 53). In the crystallographic *b*-direction, Hcy molecules were connected through H-bonds between head group NH_3^+ and COO^- as well as side-chain −SH group, thereby producing a single sheet (Fig. 1 *E, i*). Fig. 1*F* presents the top view of the H-bonded sheet. Two nearby sheets were connected to each other by further H-bonds and thus formed a single layer which can be signified as a single β-strand (Fig. 1 *E*, *ii*) (54). The monolayers packed up to form a double-layer assembly, in which side-chain to side-chain van der Waals forces connected the hydrophobic edges of the planes (Fig. 1 *E*, *iii*). A hydrophobic region was in fact composed of a bilayer, while a hydrophilic region or a single layer was composed of two hydrophilic sheets. The continuous hydrophobic stacking of single layers or supramolecular β-strands fabricated the overall packing of Hcy, which resembled supramolecular β-sheet arrangement. The H-bonding directions inside the two sheets forming a layer was the same as those in the next layer. Based on H-bonding direction, the higher-order packing of Hcy can be classified as a parallel β-sheet structure. The organization into supramolecular β-sheet structure at the atomic level further supports the amyloidal characteristics of Hcy.

Ion Mobility Spectrometry–Mass Spectrometry Analysis of Hcy Self-Assembly. Similar to the previously reported case of phenylalanine (55), the mass spectrum of Hcy (*SI Appendix*, Fig. S2) shows evidence of oligomerization under the gentle ion mobility spectrometry-mass spectrometry (IMS–MS) conditions. The IMS–MS experiments were performed in positive polarity with the fragile ion tune. The most abundant peak appeared at charge ratio (*m*/*z*) 269, indicating a singly protonated dimer (*n*/*z* = 2/1), while the protonated monomer was detected at *m*/*z* 136 (*n*/*z* = 1/1; ∼30% of the dimer) (*SI Appendix*, Fig. S2*A*). Large oligomers were assigned according to the observed mass to *m*/*z* and isotope spacings. For example, in the range from *m*/*z* 1,341 to 1,345 (*SI Appendix*, Fig. S2 *B–I*), which corresponds to a nominal oligomer to charge (*n*/*z*) of 10/1, three isotope patterns of 1.0, 0.5, and 0.33 were observed. These unique spacings suggest that there are at least three distinct populations of oligomers: singly charged decamers (*n* = 10), doubly charged eicosamers (*n* = 20), and triply charged triacontamers (*n* = 30). Following this approach, the largest oligomers identified in the mass spectrum were *n* = 36. The singly protonated oligomers were observed from *n* = 1 to 12. Doubly protonated oligomers started at *n* = 12 and at least up to *n* = 24. Triply protonated oligomers were detected at *n* = 32. Importantly, larger oligomers (*n* > 36) were not observed due to our limited mass range of fragile ion mode (*m*/*z* 100 to 1,700). Of note, we observed only even-sized oligomers in 24-h incubated samples, indicating that oligomer formation was not due to in-source clustering reactions. The exact masses of the oligomers suggest the later formation of disulfide bonds between every two Hcy monomers to stabilize the structure as the Hcy molecules are close in space (*SI Appendix*, Fig. S2*A*). In addition, some high-mass spectral peaks showed two features (conformations) in their arrival time distributions (ATDs) with the same isotope spacing, implying distinct growth paths. For example, *m*/*z* 939 with an *n*/*z* = 14/2 showed two prominent conformations (*SI Appendix*, Fig. S2 *B*, *ii*). Other mass spectral peaks with similar ATDs were *m*/*z* 1,073 (*n*/*z* = 16/2), 1,209 (*n*/*z* = 18/2), and 1,475 (*n*/*z* = 22/2).

The experimental collisional cross-sections (CCSs) were compared to different growth models, four of which were obtained from the PXRD data (*SI Appendix*, Fig. S3*A*). The models include 1) the isotropic model, commonly used in peptide assembly assuming the monomer unit and oligomers are all globular (56), 2) the monolayer formed of two Hcy sheets stabilized via intersheet hydrophilic interactions, 3) the bilayer, similar to the monolayer but made of four sheets, 4) the single-tube model where each side of the "tube" is made of three sheets, and 5) the double-tube model (*SI Appendix*, Fig. S3*B*). The isotropic model significantly deviates from the experimental data, as the monomeric Hcy is not globular. Deviations from this model were reported for other amino acids such as serine (57). The mono- and bilayer models also overestimate the CCSs. On the other hand, the single- and double-tube models better account for the growth of Hcy oligomers, as indicated by the agreement between the predicted and experimental CCSs, suggesting them to be the two growth paths for Hcy assembly. The tube models provide sufficient hydrophobic and hydrophilic stability for the growth into fibrils. Overall, our IMS–MS data provide compelling evidence that Hcy oligomerizes into fibrils via the tube modes, resembling the case of phenylalanine (55).

Kinetic Analysis of Hcy Self-Assembly. Metabolite fibrillar assemblies were previously reported to exhibit amyloid-like attributes, such as thioflavin T (ThT) binding, autofluorescence properties, and a supramolecular β-sheet–like conformation (43, 58). Here, using ThT binding assays, we could detect the kinetics of Hcy self-assembly, with higher metabolite concentrations showing stronger ThT fluorescence (Fig. 2*A* and *SI Appendix*, Fig. S4*A*).

The assembly kinetics could also be detected by the autofluorescence properties of Hcy (Fig. 2*B*), as similarly demonstrated for other metabolite assemblies (58). A ThT binding assay similarly showed a sigmoidal self-assembly of Hcy at different concentrations (Fig. 2*C*), consistent with the mechanism of nucleation growth typically observed for amyloid formation (59).

Inhibition of Hcy Fibril Formation by Polyphenols. Previous studies demonstrated that self-assembly of metabolite amyloids can be inhibited by polyphenols (48, 50). We used epigallocatechin gallate (EGCG) and tannic acid (TA), two aggregation inhibitors recently reported to inhibit fibril formation by metabolites (48, 50). We first examined the inhibitory potential of the polyphenols on Hcy self-assembly kinetics using ThT binding assays. The inhibitors were added at timepoint zero followed by monitoring of ThT fluorescence intensity (Fig. 2*D*). Both EGCG and TA were found to inhibit the formation of Hcy fibrils as reflected by the significant reduction in the ThT fluorescence intensity curves. Using TEM analysis, we confirmed that no structures were formed in the mixture of Hcy with EGCG or TA (Fig. 2 *E* and *F*) along with a control solution of Hcy alone that exhibited similar fibrils as presented in Fig. 1*A*.

Cytotoxicity of Hcy Assemblies. Previous studies demonstrated that metabolite amyloids bear a cytotoxic effect, inducing apoptotic cell death in cultured neuronal cells, similar to the effect of protein and polypeptide amyloids (43–45, 60, 61). We therefore examined the cytotoxicity and apoptotic activity of Hcy assemblies on cultured human neuroblastoma cells (SH-SY5Y) (Fig. 3). We prepared the assemblies by dissolving a wide range of Hcy concentrations in culture media. Using 3-(4,5-dimethylthiazolyl-2)-2,5-diphenyltetrazolium bromide (MTT) cell viability assay, we tested the toxicity of the assemblies following a 24-h treatment (Fig. 3*A*). Medium without Hcy that was prepared in the same manner was used as a control. As a blank, measurements of Hcy assemblies dissolved in medium at the corresponding concentration (without cells) were subtracted from the cell viability data. Hcy assemblies displayed a dose-dependent cytotoxicity and caused up to 80% cell death (Fig. 3*A*). In addition, as Hcy is part of the S-adenosyl-methionine metabolic pathway (20), we examined methionine as a negative control. We similarly prepared and treated cells with methionine solution in cell medium. The methionine solution did not show any toxicity toward the neuroblastoma cells compared to Hcy solution at the same concentration (Fig. 3*B*). Using TEM analysis, we confirmed that methionine did not form amyloid-like fibrils (*SI Appendix*, Fig. S4*C*). In addition, methionine did not show a fluorescence signal when evaluated using a ThT assay and compared to Hcy (*SI Appendix*, Fig. S4*B*). Notably, no significant toxicity was observed toward a nonneuronal HEK293 cell line (*SI Appendix*, Fig. S5*A*), suggesting cell-type–dependent toxicity.

We further examined the cytotoxicity toward SH-SY5Y cells following inhibition of Hcy self-assembly by EGCG and TA. The inhibitors were added to the Hcy solutions prepared in cell media before gradual cooling. As described above, we treated SH-SY5Y

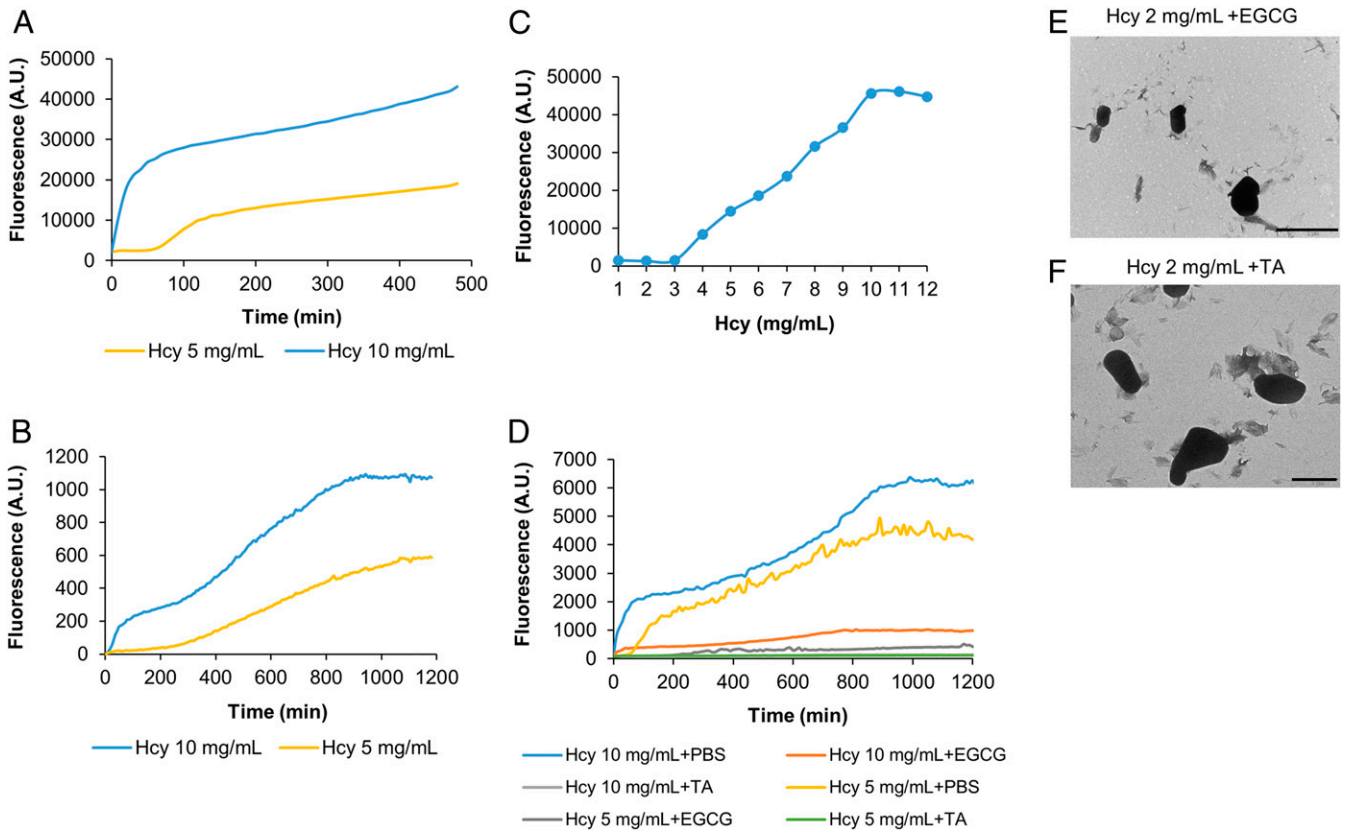

Fig. 2. Kinetic analysis of Hcy self-assembly and inhibition by polyphenols. (*A*) Kinetic analysis of Hcy self-assembly at the indicated concentrations detected using a ThT binding assay. ThT emission data at 480 nm (excitation at 440 nm) were measured over time. (*B*) Kinetic analysis of Hcy self-assembly at the indicated concentrations detected by autofluorescence intensity over time (excitation at 375 nm, emission at 450 nm). (*C*) Hcy self-assembly at different concentrations. Hcy was dissolved to a final concentration of 1 to 12 mg/mL. Using a ThT binding assay, the fluorescence emission endpoint was measured at 480 nm (excitation at 450 nm). (*D*) Inhibition of Hcy self-assembly by polyphenols. Hcy at the indicated concentrations was mixed with the inhibitors (1 mM EGCG or 0.1 mM TA) at timepoint zero, or with PBS as a control, followed by addition of ThT. ThT emission data at 480 nm (excitation at 440 nm) were measured over time. (*E* and *F*) TEM micrographs of preformed solutions of Hcy with polyphenols. (*E*) Hcy-2 mg/mL + 1 mM EGCG. (*F*) Hcy-2 mg/mL + 0.1 mM TA. (Scale bar, 1 μm.)

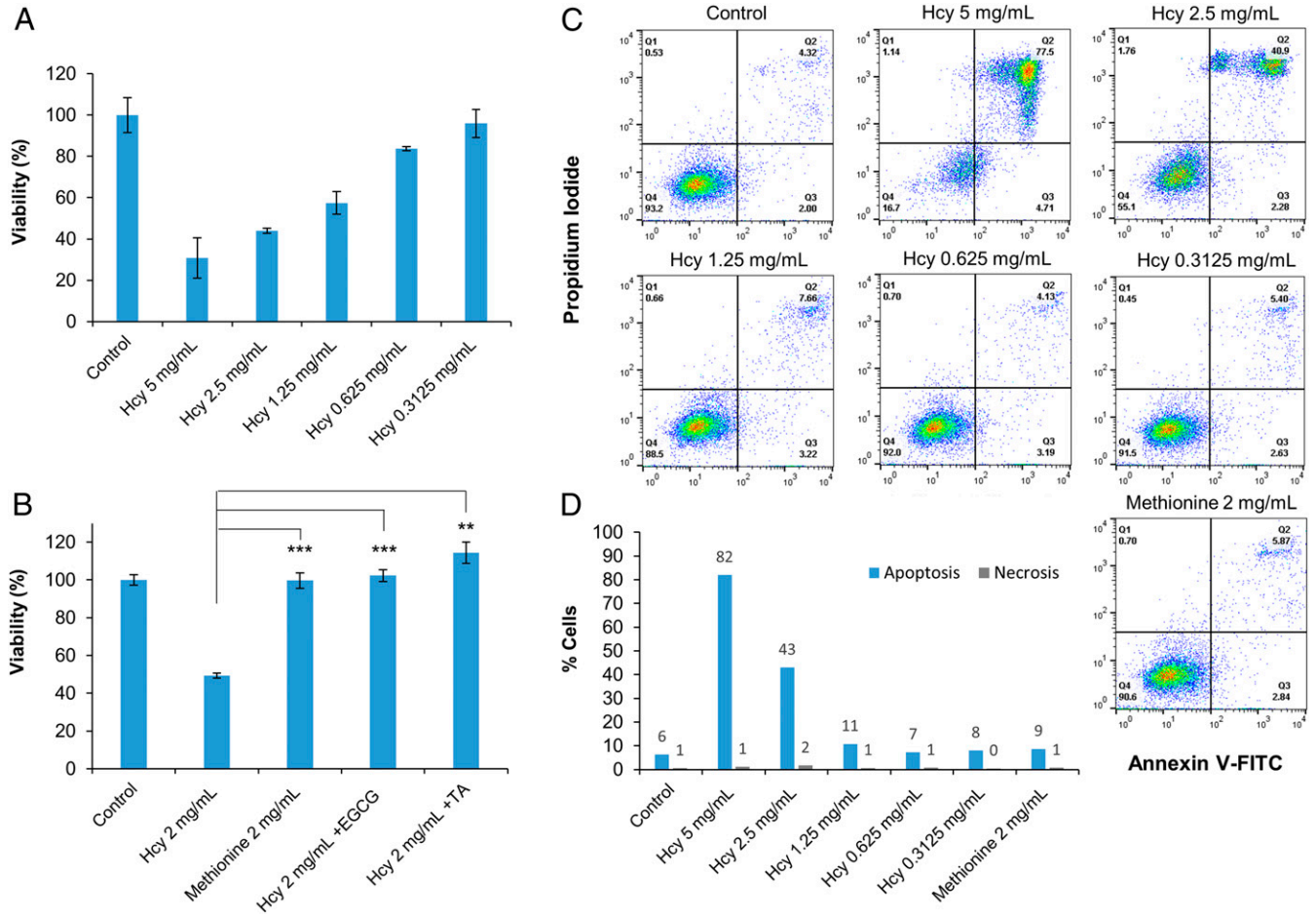

Fig. 3. Cytotoxicity of Hcy assemblies. (*A*) Cytotoxicity of Hcy assemblies as determined by MTT cell viability assay. Treated SH-SY5Y cells were incubated with preformed Hcy assemblies prepared in cell medium for 24 h. The control reflects medium without Hcy, which was treated in the same manner. Absorbance was determined at 570/680 nm. (*B*) Cytotoxicity of Hcy assemblies tested following self-assembly inhibition by polyphenols and cytotoxicity of methionine as a control. Hcy assemblies (2 mg/mL) were similarly prepared in cell medium in the presence of EGCG (0.1 mM) or TA (0.01 mM). Methionine solution was similarly prepared in cell medium. The control reflects medium with no metabolites, which was treated in the same manner. Treated SH-SY5Y cells were incubated with the solutions for 24 h followed by MTT cell viability assay. (**$P < 0.01$, ***$P < 0.001$ Student's *t* test). (*C* and *D*) Apoptotic activity studied by annexin V and PI assay. SH-SY5Y cells were treated as described for MTT assay. After incubation, annexin V-FITC and PI were added to the cells, followed by flow cytometry analysis using a single laser–emitting excitation light at 488 nm. (*C*) Flow cytometry plots of the annexin V-FITC/PI double-staining assay. Q1, PI(+) (cells undergoing necrosis); Q2, annexin V-FITC(+) PI(+) (cells in late apoptosis and undergoing secondary necrosis); Q3, annexin V-FITC(+) PI(−) (cells in early apoptosis); and Q4, annexin V-FITC(−) PI(−) (live cells). (*D*) Quantification of the flow cytometry results; apoptosis is represented in blue (early + late apoptosis) and necrosis in gray.

cells with cell media containing Hcy that was supplemented with EGCG or TA for 24 h (Fig. 3*B*). When treating cells with inhibitors-containing solutions, the MTT assay indicated a significant increase in cell viability compared to Hcy solutions in the absence of EGCG or TA (Fig. 3*B*). We further verified that the inhibitors alone did not affect cell viability (*SI Appendix*, Fig. S5*B*). These results validate the amyloid-like properties of Hcy fibrils and confirm Hcy structures, rather than an osmotic effect, as the toxicity-causing agent.

Next, we examined whether the cytotoxicity of Hcy fibrils was due to apoptotic cell death. We used annexin V and propidium iodide (PI) labeling, followed by flow cytometric analysis (Fig. 3 *C* and *D*). Different concentrations of Hcy assemblies as well as methionine solution in cell media were prepared as described above, and cultured SH-SY5Y cells were treated for 24 h. The Hcy assemblies caused cell death and stimulated apoptotic activity in a concentration-dependent manner, while the methionine negative control did not show any apoptotic effect, as indicated by annexin V and PI assay (Fig. 3 *C* and *D*). These results demonstrate that apoptosis, rather than necrosis, was the main triggered pathway causing SH-SY5Y cell death following treatment with Hcy assemblies.

Detection of Amyloid-like Structures in SH-SY5Y Cells. Following the observed cytotoxicity, we sought to detect Hcy amyloid–like fibrils in treated SH-SY5Y cells. The cells were stained with the Proteo-Stat amyloid-specific fluorescent dye which was recently shown to be indicative of intracellular amyloid fibrils in yeast (48). We similarly prepared solutions of Hcy assemblies (2 mg/mL) by dissolving the metabolite in cell culture medium followed by treatment of SH-SY5Y cells for 4 h. Medium without Hcy that was prepared in the same manner was used as a control. The treated and untreated cells were observed using confocal microscopy (*SI Appendix*, Fig. S6), demonstrating the amyloid-like structures in treated SH-SY5Y cells while no staining was detected in the untreated cells.

In Vivo Yeast Model for Hcy Toxicity. Next, we sought to establish an in vivo model for the study of Hcy accumulation and toxicity. The budding yeast *Saccharomyces cerevisiae* has been successfully used as a model organism for the study of metabolite aggregation,

as well as of amyloid-associated diseases (48, 49). We therefore aimed to establish a *S. cerevisiae* model of Hcy accumulation. Based on the etiology of hyperhomocysteinemia (28, 29), a knockout mutation in *CYS4*, the highly conserved functional yeast CBS ortholog, was constructed (see *Materials and Methods*). Due to the contribution of *CYS4* to cysteine biosynthesis (62), its absence conferred cysteine dependence (Fig. 4*A*). Indeed, sensitivity to Hcy supplied in the growth medium was observed in the Hcy salvage model compared to the wild-type (WT) strain in a dose-dependent manner (Fig. 4 *B* and *C*). To examine whether the observed toxicity was associated with the formation of amyloid-like assemblies in vivo, cells were stained with the amyloid-specific fluorescent dye ProteoStat. Upon Hcy feeding, a significantly higher degree of aggregation was detected by flow cytometry in the mutant compared to WT cells as well as compared to the mutant strain in the absence of Hcy, indicating the presence of amyloid-like structures in the Hcy salvage mutant (Fig. 4 *D* and *E*). Confocal microscopy imaging of the stained cells provided additional observation of the formation of amyloid-like assemblies in vivo (*SI Appendix*, Fig. S7). Next, the yeast model was used to validate the rescue of cytotoxicity by the polyphenol TA, as observed in cultured human neuroblastoma cells. While no effect was observed in the WT strain, the addition of TA significantly improved the cell growth of the mutant strain (Fig. 4*F*).

Hcy and β-Amyloid Interplay in Brain Sections of AD Model Mice. Many studies show a clear link between Hcy accumulation in serum and AD pathology, as well as Hcy toxicity toward hippocampal and cortical neurons and toward astrocytes (35–37, 63, 64). To test the presence of Hcy fibrils in vivo and to further search for a possible cross-talk with pathological proteins, we examined whether Hcy fibrils could be detected in brain sections of AD model mice. We immunostained brain sections of WT and AD model mice [5XFAD, 13 mo (65, 66)] using a rabbit anti–Hcy-fibrils antibody we developed (*SI Appendix*) and two additional commercial anti–monomeric-Hcy antibodies (*SI Appendix*, Fig. S8). Among the three, only our rabbit anti–Hcy-fibrils antibody could detect Hcy in brain sections of AD model mice (Fig. 5 and *SI Appendix*, Fig. S8*B*), demonstrating the formation of Hcy assemblies in vivo. WT sections stained with anti-Hcy antibodies did not show any signal, suggesting a clear link between Hcy fibril formation and AD pathology (Fig. 5*A* and *SI Appendix*, Fig. S9). In parallel, we immunostained the same sections with anti–β-amyloid$_{1\text{-}42}$ antibody (6E10) (Fig. 5 *C*–*F* and *SI Appendix*, Fig. S8) or an antibody for anti-glial fibrillary acidic protein (GFAP), which is highly expressed in astrocytes (Fig. 6). In AD model mice, both β-amyloid$_{1\text{-}42}$ and astrocytes could be detected (Figs. 5*D* and 6*B*). Furthermore, we could observe a correlation between detected Hcy fibrils and β-amyloid$_{1\text{-}42}$ aggregation (Fig. 5*F*) as well as colocalization of Hcy fibrils with the

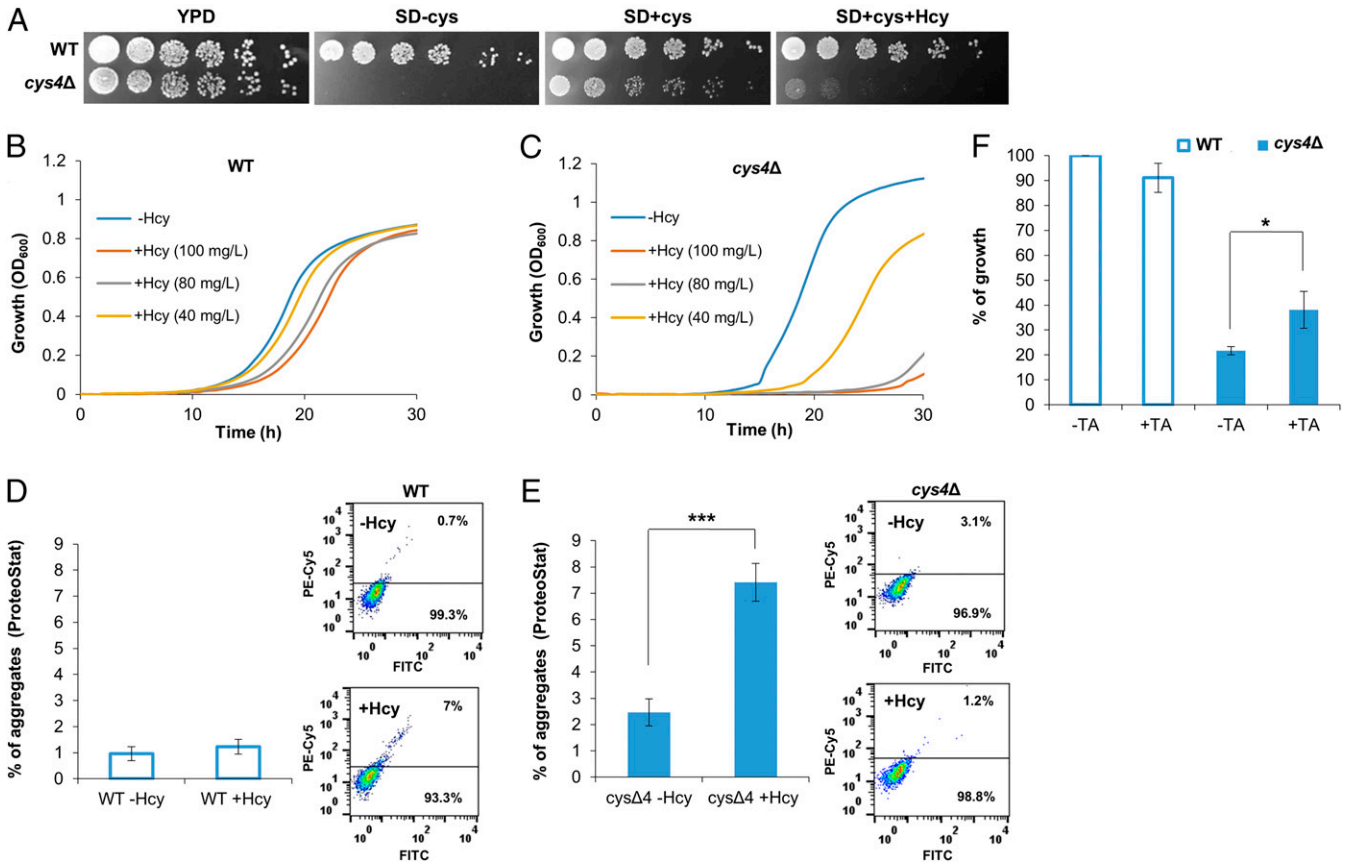

Fig. 4. Yeast model for Hcy accumulation and toxicity. (*A*) WT and *cys4*Δ strains were serially diluted and spotted on yeast extract peptone dextrose (YPD) medium, synthetic defined (SD) medium containing 13 mg/L cysteine and 100 mg/L Hcy (SD + cys + Hcy), SD medium without cysteine and Hcy (SD-cys) or SD medium containing 13 mg/L cysteine without Hcy (SD+cys). (*B* and *C*) Growth curves of (*B*) WT and (*C*) *cys4*Δ on SD media with or without Hcy at different concentrations (40 mg/L, 80 mg/L, and 100 mg/L). (*D* and *E*) Flow cytometry analysis of (*D*) WT and (*E*) *cys4*Δ strains grown in SD media containing 13 mg/L cysteine and 100 mg/L Hcy or without Hcy, using ProteoStat staining. The graphs represent quantification of the flow cytometry results presented in the histograms. (*F*) WT and *cys4*Δ strains diluted to OD_{600} 0.01 were grown in SD media containing 13 mg/L cysteine and 100 mg/L Hcy, with or without 0.3 mM TA. The percentage of growth was calculated as the growth under the indicated condition compared to the growth of WT without TA (*$P < 0.05$, ***$P < 0.001$ Student's *t* test).

astrocytes (Fig. 6*C*), while WT sections showed a positive staining of astrocytes but no β-amyloid$_{1-42}$ signal, as expected (Figs. 5*C* and 6*E* and *SI Appendix*, Fig. S9).

Seeding of β-Amyloid$_{1-42}$ by Hcy Assemblies. Following the observed correlation in the distribution of Hcy and β-amyloid and as the exacerbation of β-amyloid–induced toxicity by Hcy has already been reported in previous studies (35–37, 61), we investigated the ability of Hcy assemblies to directly cross-seed the aggregation of β-amyloid$_{1-42}$. Monomeric β-amyloid$_{1-42}$ was coincubated with preformed Hcy assemblies and protein aggregation was monitored using a ThT binding assay (*SI Appendix*, Fig. S10). We found that Hcy seeds induced β-amyloid$_{1-42}$ aggregation in a concentration-dependent manner, with higher concentrations of the preformed Hcy assemblies resulting in a higher ThT signal. Samples of β-amyloid$_{1-42}$ in the absence of Hcy assemblies showed a significantly lower fluorescence signal (*SI Appendix*, Fig. S10).

Discussion

We describe here the formation of amyloid-like structures by Hcy, a sulfur-containing noncoded amino acid, which is involved in numerous maladies including neurodegenerative diseases (20, 30, 67). Our results decipher the previously unknown X-ray structure of Hcy and present a characterization of its self-assembly into cytotoxic amyloid-like fibrils. We further establish a yeast model of Hcy aggregation and toxicity. Notably, the in vivo yeast model recapitulates both the cell toxicity observed in cultured human cells and the rescue of toxicity by a known inhibitor of amyloid formation. The yeast model may thus serve as a platform to screen for potential inhibitory compounds using high-throughput screening methods (49). Finally, we demonstrate the presence of Hcy assemblies in brain sections of AD model mice but not in the brains of WT animals in colocalization with astrocytes as well as their correlation with β-amyloid$_{1-42}$ aggregation. This is consistent with the previously reported occurrence of Hcy in astrocytes but provides immunohistochemical indication for the aggregative state of the metabolite (68). Following this striking observation, and as the epidemiological association between Hcy and AD-related pathological proteins is well established (35, 36, 38, 39, 61), we further investigated the ability of Hcy assemblies to cross-seed the aggregation of β-amyloid$_{1-42}$, and indeed, an induced aggregation of the pathological protein could be observed. This result is in agreement with other observations regarding protein aggregation seeded by metabolite assemblies (45, 46, 69). Our data suggest a dual role for Hcy assemblies in AD pathology. First, Hcy fibrils may induce cytotoxicity via apoptotic cell death. Second, Hcy assemblies may cross-seed the aggregation of β-amyloid$_{1-42}$, resulting in the formation of toxic protein amyloid structures. The interplay between the two mechanisms should be further examined, as well as the effect of inhibitory compounds impeding Hcy assembly. We propose metabolite–protein cross-talk as an interesting possible mechanism for the initiation of neurodegenerative pathologies.

CBS and 5,10-methylenetetrahydrofolate reductases are key enzymes in Hcy metabolism. Mutations and polymorphism in the

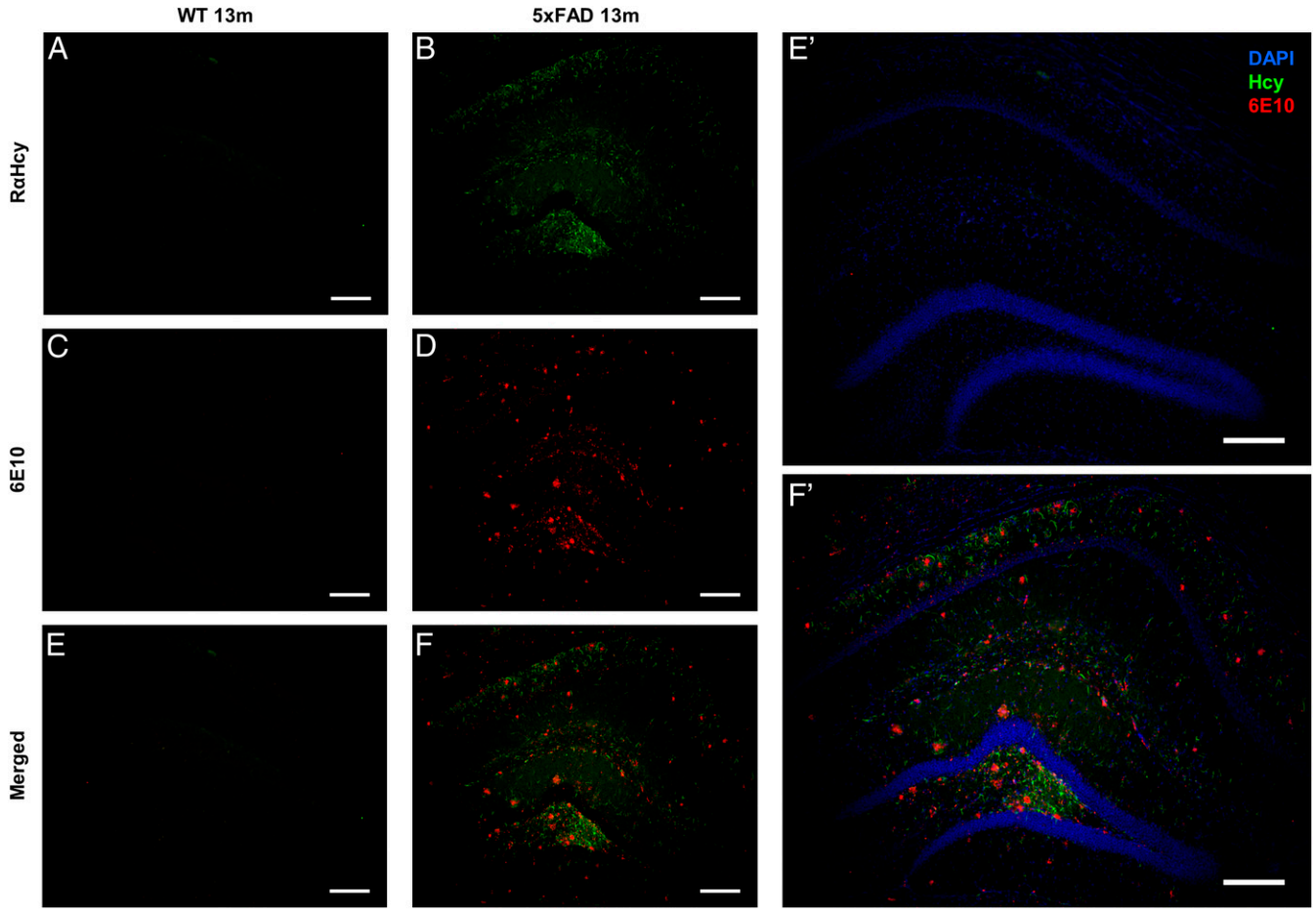

Fig. 5. Detection of Hcy fibrils correlates with β-amyloid$_{1-42}$ aggregation in AD model mice. The images represent sections of 5xFAD or WT animals. (*A* and *B*) Sections stained with anti–Hcy-fibrils antibodies (green). (*C* and *D*) Sections stained with anti–β-amyloid$_{1-42}$ antibody 6E10 (red). (*E* and *F*) Merge of Hcy and β-amyloid$_{1-42}$ staining. (*E′* and *F′*) Enlarged images of *E* and *F*, respectively, merged with DAPI staining. (Scale bar, 200 μm.)

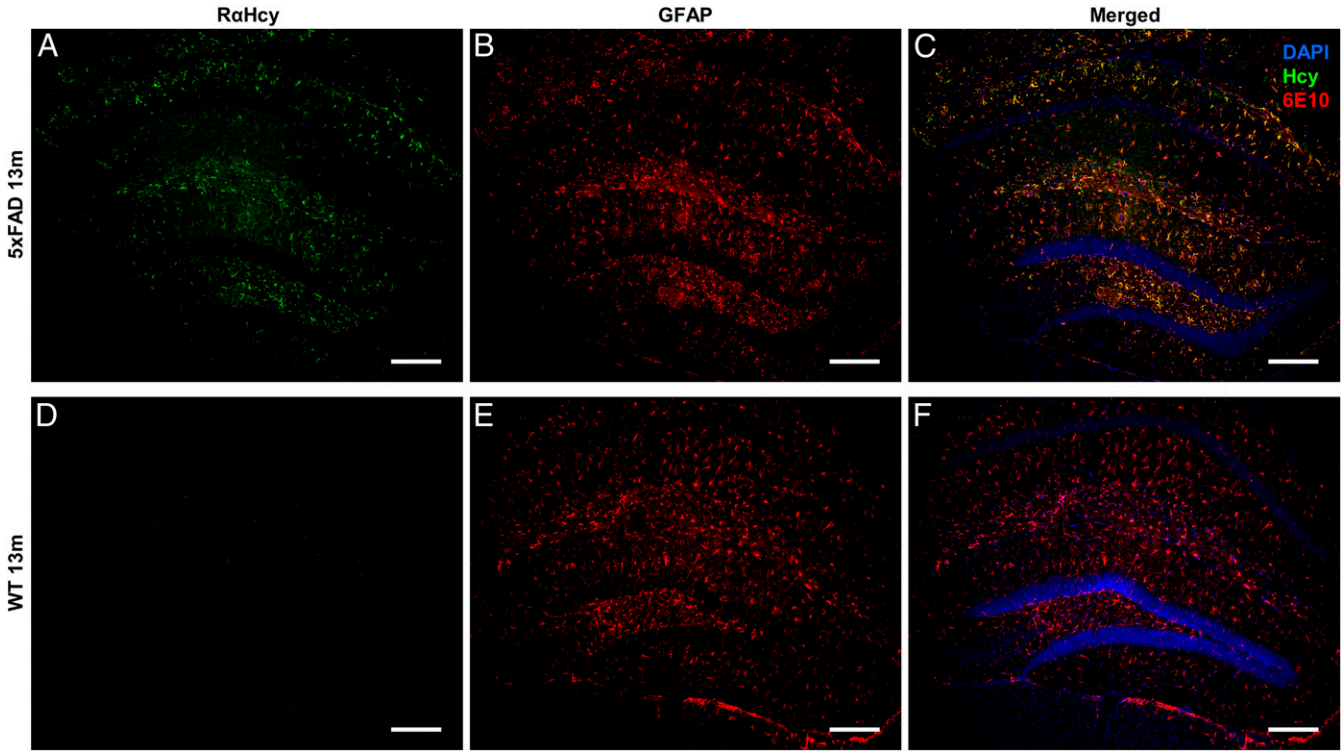

Fig. 6. Detection of Hcy fibrils and colocalization with astrocytes in AD model mice. The images represent sections of (*A–C*) 5xFAD or (*D–F*) WT animals. (*A* and *D*) Sections stained with anti–Hcy-fibrils antibodies (green). (*B* and *E*) Sections stained with anti-GFAP antibodies (red). (*C* and *F*) Merge of Hcy and GFAP staining with DAPI staining. (Scale bar, 200 μm.)

genes encoding these enzymes are common in the Caucasian population, reaching up to 2 to 10% (28, 67, 70, 71). Subjects carrying these alleles have an elevated risk to develop AD yet are considered "sporadic" despite the relevant genetic background. Along with AD, high levels of Hcy are involved in many other diseases, such as diabetes (72), neurological diseases (67), vascular diseases (73), age-related macular degeneration (74), cancer (75), and hearing loss (76). Thus, the formation of amyloid-like fibrils by Hcy, their toxicity, and cross-seeding capability are highly relevant to many biological and medicinal fields. Additional study of the presence of Hcy fibrils (e.g., in human body fluids) and their role in diverse pathological processes is essential and may contribute to the identification and prevention of AD and many other illnesses.

Materials and Methods

Materials. L-Homocysteine was purchased from CHEM-IMPEX with purity ≥98%. Other materials (methionine, EGCG, and TA) were purchased from Sigma. Fresh stock solutions were prepared by dissolving the metabolites at 90 °C in phosphate buffered saline (PBS) or Dulbecco's modified Eagle's medium (DMEM)/Nutrient Mixture F12 (Ham's 1:1, Biological Industries, without fetal bovine serum [FBS]) at various concentrations, followed by gradual cooling of the solutions.

TEM. Hcy was dissolved at 90 °C in PBS at various concentrations followed by gradual cooling of the solution. Where indicated, EGCG or TA (final concentration of 1 and 0.1 mM, respectively) were added before gradual cooling. Subsequently, 10-μL samples were placed on 400-mesh copper grids. After 2 min, excess fluids were removed. Samples were viewed using a JEOL 1200EX electron microscope operating at 80 kV.

cryo-TEM. Hcy solutions were prepared as described for TEM. Vitrified specimens were prepared on a copper grid coated with a perforated lacy carbon 300 = mesh (Ted Pella Inc.). A 3-μL drop from the solution was applied to the grid and blotted with a filter paper to form a thin liquid film of solution. The blotted sample was immediately plunged into liquid ethane at its freezing point (−183 °C). The procedure was performed automatically in the Plunger (Leica electron microscope grid plunger). The vitrified specimens were transferred into liquid nitrogen for storage. The samples were analyzed using a FEI Tecnai 12 G2 TEM, at 120 kV with a Gatan cryo-holder maintained at −180 °C, and images were recorded on a slow scan cooled charge-coupled device camera (Gatan). Images were recorded using the Digital Micrograph software package, at low-dose conditions, to minimize electron beam radiation damage. Measurements were performed at the Ilse Katz Institute for Nanoscale Science and Technology (Ben-Gurion University of the Negev).

PXRD. Lyophilized Hcy powder was dissolved to a concentration of 2 mg/mL in double-distilled water and allowed to self-assemble by incubating at 18 °C for 1 wk. The sample was then centrifuged for 10 min at 6,000 rpm and the solution was decanted to remove nonassembled molecules. The assembled fibers were lyophilized and poured inside a glass capillary 0.7 mm in diameter. X-ray diffraction was collected using a Bruker D8 Discover diffractometer with LYNXEYE EX linear position detector. The capillary setup employed was as follows: Göbels mirrors to obtain a parallel beam, rotating capillary holder and 2 ϑ scan between 2 and 50°, step 0.02 Å. The presence of three NaCl peaks was noticed in the diffraction pattern. As it was not possible to obtain a sample without the presence of NaCl, these peaks were excluded in the further data treatments. Crystallographic structure determination was performed using the EXPO2014 software (77). EXPO2104 was used with cell indexing (N-TREOR09 algorithm) and the Simulated Annealing Method.

The solution with the lowest Cost Function was used as model to perform further crystal refinement on the structure using the GSASII software (78). The final error indexes were: weighted R factor = 5.83% and goodness of fit = 3.46. The crystallographic data have been deposited in the Cambridge Crystallographic Data Centre with no. 1976215.

ThT Kinetics Assay. Hcy was dissolved at 90 °C in PBS to a final concentration of 10, 5, and 2 mg/mL and maintained at 90 °C until the beginning of the measurement. Samples containing polyphenols were immediately mixed with the inhibitors, EGCG or TA (final concentration of 1 and 0.1 mM, respectively). As a control, Hcy was diluted with PBS alone to the same final concentrations. ThT in PBS was added to a final concentration of 20 μM for 5 and 10 mg/mL Hcy or 40 μM for 2 mg/mL Hcy. Next, the solutions were plated

in a black 96-well, clear, and flat-bottom microplate (Greiner) and self-assembly kinetics were recorded over time at room temperature (uncontrolled gradual cooling of the solutions) with short shaking before each read. ThT emission data at 480 nm (excitation at 440 nm) were measured using a Tecan SPARK 10M plate reader, gain of 100 for 2 mg/mL Hcy, and using a Tecan Infinite 200 PRO plate reader, gain of 90 for 5 and 10 mg/mL Hcy. The displayed results are representative of three experiments performed in triplicates.

Autofluorescence Kinetics Assay. Hcy was dissolved at 90 °C in PBS to a final concentration of 10 and 5 mg/mL and maintained at 90 °C until the beginning of the measurement. Next, the solutions were plated in a black 96-well, clear, and flat-bottom microplate (Greiner) and self-assembly kinetics were recorded over time at room temperature (uncontrolled gradual cooling of the solutions) with short shaking before each read. Emission data at 450 nm (excitation at 375 nm) were measured using a Tecan SPARK 10M plate reader. The displayed results are representative of three experiments performed in triplicates.

ThT Fluorescence Endpoint Measurements. Hcy was dissolved at various concentrations, ranging from 1 to 12 mg/mL, at 90 °C in PBS and plated on a 96-well black plate together with 20 μM ThT in PBS (final concentration). Following an overnight incubation at room temperature with gentle rotation (uncontrolled gradual cooling of solutions), ThT emission signal at 480 nm (excitation at 450 nm) was measured at room temperature with short shaking before each read and using a Tecan Infinite 200 PRO plate reader, gain 90. The displayed results are representative of three experiments performed in triplicates.

Cytotoxicity Experiments. SH-SY5Y cells (ATCC CRL-2266) or HEK293 cells (ATCC CRL-1573) were cultured (2×10^5 cells/mL) in DMEM/Nutrient Mixture F12 (Ham's; 1:1) supplemented with 10% FBS in 96-well tissue microplates (100 μL per well) and allowed to adhere overnight at 37 °C. Half of each plate was plated with cells, with the other half later serving as a control containing solutions alone. The treatment solutions were prepared as follows: Hcy or methionine were dissolved at 90 °C and at various concentrations in cell media without FBS, followed by gradual cooling of the solutions. For solutions containing polyphenols, Hcy (final concentration of 2 mg/mL) was similarly dissolved in cell media and mixed with EGCG or TA (final concentration of 0.1 and 0.01 mM, respectively, stock solution dissolved in cell medium) before gradual cooling. The medium was replaced, and cells were treated with the solutions (100 μL per well), followed by overnight incubation at 37 °C. Control cells were incubated with medium that was treated in the same manner (without Hcy). Controls of media supplemented with the inhibitors, without Hcy, were examined as well. Cell viability was evaluated using the MTT assay. Briefly, 10 μL of 5 mg/mL MTT dissolved in PBS was added to each well. After a 4 h incubation at 37 °C, 100 μL extraction buffer [20% sodium dodecyl sulphate dissolved in a mixture of 50% dimethylformamide and 50% double distilled water (pH 4.7)] was added to each well, and the plates were further incubated at 37 °C for 30 min. Finally, color intensity was measured using a plate reader at 570 nm. Blank measurements of the solutions without cells were respectively subtracted. The data points are presented as mean ± SD. For inhibitors and methionine controls, two-tailed Student's *t* test was performed when two groups were compared. The displayed results are representative of three biological experiments performed in triplicates.

Apoptosis Assay. SH-SY5Y cells were cultured at 2×10^5 cells/mL in 24-well plates in DMEM/Nutrient Mixture F12 (Ham's; 1:1) supplemented with 10% FBS and were allowed to adhere overnight at 37 °C. The treatment solutions containing Hcy and methionine were prepared as described above for the MTT assay. Cells were treated with the solutions followed by overnight incubation at 37 °C. Control cells were incubated with medium that was treated in the same manner without Hcy. The apoptotic effect was evaluated using the MEBCYTO Apoptosis kit (MBL International), according to the manufacturer's instructions. Briefly, the adherent cells were trypsinized, detached, and combined with floating cells from the incubated growth medium. Cells were then centrifuged and washed once with PBS and once with binding buffer. Cells were subsequently incubated with annexin V-FITC and PI for 15 min in the dark, resuspended in 200 μL binding buffer and analyzed by flow cytometry using a single laser–emitting excitation light at 488 nm. Data from at least 10^4 cells were acquired using the BD FACSort and the CellQuest software (BD Biosciences). Analysis was performed using the FlowJo software (TreeStar, version 14). The displayed results are representative of three biological experiments performed in triplicates.

Construction of *cys4*Δ Yeast Strain. The *cys4* gene was disrupted in WT yeast strain (BY4741) via homologous recombination using PCR fragments amplified from the plasmid pFA6a-KanMX6 as a template with primer DL154: (5′GATTTCGTTGTAGGCCACTTGCTCAAAGGACATCTAGATAAATACGACGTAAGAATAAAACGGATCCCCGGGTTAATTAA-3′) and primer DL155: (5′AGGAAAGGAATGACGGATTTTGCTTCTATGTTTGCTTTTATTTGAAGCGTGGGTTCTTATACATTTGATTAAAATAGAAC-3′) where underlining indicates the plasmid sequence. Gene replacement was validated by PCR with suitable primers.

Yeast Growth Assays. WT and *cys4*Δ strains were grown overnight at 30 °C. Unless otherwise specified, the strains were grown on synthetic defined medium containing 20 mg/L L-methionine, 20 mg/L L-histidine monohydrochloride monohydrate, 20 mg/L uracil and 30 mg/L L-leucine. Cysteine was added to a final concentration of 13 mg/L. Hcy was added at the indicated concentrations.

For spotting assays, strains were diluted to 6.25×10^7 cells/mL and then fivefold serially diluted and spotted on the indicated plates. Plates were incubated at 30 °C for 2 to 3 d. The displayed results are representative of three biological experiments.

For optical density at 600 nm (OD_{600}) measurements, strains were diluted to OD_{600} 0.01. A total of 200 μL cells were platted on 96-well plates and incubated at 30 °C for 30 h with continuous shaking. OD_{600} was measured using Tecan SPARK 10M plate reader. The displayed results are representative of three biological experiments performed in triplicates.

The percentage of growth analysis (Fig. 4*F*) represents the OD_{600} levels following 27 h of growth in the plate reader. The percentage of growth represents the growth under the indicated conditions, with or without 0.3 mM TA, compared to the growth of WT without TA. The displayed results are representative of three biological experiments performed in triplicates.

Aggregation Level Assays in Yeast. For each sample, 2×10^6 cells/mL of logarithmic cells were resuspended with ProteoStat dye (Enzo Life Sciences). Cells were incubated for 15 min at room temperature protected from light. Flow cytometry was preformed using Stratedigm S1000EXi and the CellCapTure software (Stratedigm). Live cells were gated (P1) by forward scatter and side scatter. Fluorescence channels for FITC (530/30) and PE-Cy5 (676/29) were used utilizing a 488-nm laser source. A total of 50,000 events were acquired for each sample. Analyses were performed using the FlowJo software (TreeStar, version 14). The displayed results are representative of three biological experiments performed in triplicates.

Mouse Model of AD. 5xFAD model mice co-overexpress a familial AD (FAD) mutant form of human amyloid precursor protein and human Presenilin1 (PS1). These double-transgenic mice coexpress five FAD mutations (5XFAD mice: the Swedish mutation, K670N/M671L; the Florida mutation, I716V; the London mutation, V717I, and PS1 M146L/L286V transgenes) which increase β-amyloid production. β-amyloid deposition is first detected in the brain of the model mice in the subiculum of the hippocampal area. Mice develop β-amyloid plaques (and gliosis) by 5 to 6 wk of age, show robust inflammation and neuronal damage, and reach a very large plaque burden, especially in the subiculum and deep cortical layers (65, 66). Studies were performed using three 13-mo-old 5xFAD female mice and three age-matched WT female mice.

All mice were euthanized using CO_2 and intracardially perfused with Ringer's solution (NaCl 6.5 gL^{-1}, KCl 0.42 gL^{-1}, $CaCl_2$ 0.25 gL^{-1}, and $NaHCO_3$ gL^{-1}, containing 4 units mL^{-1} of Heparin in distilled water) followed by 4% paraformaldehyde (PFA) in PBS. Brains were collected and postfixed with 4% PFA overnight at 4 °C before treated by a sucrose gradient: 15% sucrose in PBS overnight followed by 30% sucrose in PBS overnight. Brains were preserved in Peel-A-Way disposable plastic tissue-embedding molds (Sigma no. E6032) filled with tissue freezing media (optimal cutting temperature compound) and stored at −80 °C until sectioning. Coronal tissue sections (20-μm thick) were obtained using Leica CM 1950 Cryostat. Sections were placed on glass slides, air dried, and kept at −20 °C until staining. All experiments were in accordance with Tel Aviv University guidelines and approved by the Tel Aviv University Institutional Animal Care and Use Committee (protocol no. 04-17-033).

Immunohistological Staining of Mouse Brain Tissue. Samples were washed three times in PBS (3 × 5 min), fixed with 4% PFA (in PBS) for 10 min, washed (3 × 5 min) in PBS, and then permeabilized for 10 min in 0.5% Triton X-100 (Sigma-Aldrich) in PBS. The slices were blocked with a blocking solution containing 0.5% Triton, 0.3 M glycine, 1% bovine serum albumin (BSA) solution in PBS for 1 h, then incubated with primary rabbit anti–Hcy-fibrils

antibodies overnight at 4 °C (purified by Adar Biotech; 1:200 in blocking solution) or similarly with commercial antibodies from Abcam (no. ab15154) and Sigma-Aldrich (no. AB5512). On the next day, the samples were washed three times in PBS and incubated with Alexa F488–conjugated goat anti-rabbit secondary antibody diluted 1:500 in PBS for 1 h at 25 °C (ThermoFisher; no. A11008).

For double immunofluorescence staining, the same sections were washed with PBS (3 × 5 min), blocked again with a blocking solution containing 8% (vol/vol) horse serum, 0.3% (vol/vol) Triton, 1% (wt/vol) BSA, and 0.02% (vol/vol) sodium azide solution (in PBS) for 1 h, and then incubated with primary mouse anti–A-β antibodies (6E10, BioLegend; no. 803001) or primary rat anti-GFAP antibodies (GFAP, Millipore; no. 345860) diluted 1:500 in blocking solution, overnight at 4 °C. After washing (PBS 3 × 5 min), the sections were incubated with Alexa F594–conjugated goat anti-mouse (ThermoFisher; no. A11005) or goat anti-rat (ThermoFisher; no. A11007) secondary antibody diluted 1:500 in PBS, for 1 h at 25 °C, and costained with DAPI diluted 1:500 in PBS for 10 min to detect nuclei (DAPI, Sigma-Aldrich). Sections were then mounted in Vectashield mounting medium (Vector Labs) and coverslipped. Immunofluorescence-stained brain sections were observed, and images were acquired at ×10 magnification using Nikon Eclipse 80i fluorescence microscope and MicroPublisher 6 camera (Teledyne QImaging). The displayed results are representative of three independent biological repeats.

Data Availability. All study data are included in the article and/or *SI Appendix*.

ACKNOWLEDGMENTS. We thank Dr. S. Rencus-Lazar for proofreading the article and Dr. E. Nativ-Roth for assisting in cryo-TEM analysis at Ben-Gurion University. We thank Dr. S. Lichtenstein for microscopy analysis and fruitful discussions, Dr. O. Sagi-Assif for the fluorescence-activated cell sorting analysis, and members of the E.G. group for helpful discussions. We thank Myra Gartner for great assistance with yeast experiments. D.S.O. and T.D.D. gratefully acknowledge the laboratory startup research support from the University of Tennessee and the Department of Chemistry and the Global Academic Support Program from Agilent. This work was supported by the Israel Science Foundation (Grant No. 1558/19 to E.G.), the Adelis Forever Foundation to E.G., and the Prajs-Drimmer Institute for Anti-Degenerative Drugs and the Aufzien Family Center for the Prevention and Treatment of Parkinson's Disease to D.S.Y. and E.G. Part of this work was supported by Israel Science Foundation Grant No. 1365/19 (to D.F.).

1. C. Reitz, R. Mayeux, Alzheimer disease: Epidemiology, diagnostic criteria, risk factors and biomarkers. *Biochem. Pharmacol.* **88**, 640–651 (2014).
2. Alzheimer's Association, 2015 Alzheimer's disease facts and figures. *Alzheimers Dement.* **11**, 332–384 (2015).
3. J. Meldolesi, Alzheimer's disease: Key developments support promising perspectives for therapy. *Pharmacol. Res.* **146**, 104316 (2019).
4. S. R. Chandra, Alzheimer's disease: An alternative approach. *Indian J. Med. Res.* **145**, 723–729 (2017).
5. F. Chiti, C. M. Dobson, Protein misfolding, functional amyloid, and human disease. *Annu. Rev. Biochem.* **75**, 333–366 (2006).
6. D. Eisenberg, M. Jucker, The amyloid state of proteins in human diseases. *Cell* **148**, 1188–1203 (2012).
7. M. Citron *et al*., Mutation of the β-amyloid precursor protein in familial Alzheimer's disease increases β-protein production. *Nature* **360**, 672–674 (1992).
8. Z. Amtul, Why therapies for Alzheimer's disease do not work: Do we have consensus over the path to follow? *Ageing Res. Rev.* **25**, 70–84 (2016).
9. E. Karran, B. De Strooper, The amyloid cascade hypothesis: Are we poised for success or failure? *J. Neurochem.* **139**, 237–252 (2016).
10. F. Pistollato *et al*., Alzheimer disease research in the 21st century: Past and current failures, new perspectives and funding priorities. *Oncotarget* **7**, 38999–39016 (2016).
11. J. A. Hardy, G. A. Higgins, Alzheimer's disease: The amyloid cascade hypothesis. *Science* **256**, 184–185 (1992).
12. T. P. J. Knowles, M. Vendruscolo, C. M. Dobson, The amyloid state and its association with protein misfolding diseases. *Nat. Rev. Mol. Cell Biol.* **15**, 384–396 (2014).
13. G. G. Glenner, C. W. Wong, Alzheimer's disease: Initial report of the purification and characterization of a novel cerebrovascular amyloid protein. *Biochem. Biophys. Res. Commun.* **120**, 885–890 (1984).
14. C. A. Ross, M. A. Poirier, Protein aggregation and neurodegenerative disease. *Nat. Med.* **10**, S10–S17 (2004).
15. E. Socha, M. Koba, P. Kośliński, Amino acid profiling as a method of discovering biomarkers for diagnosis of neurodegenerative diseases. *Amino Acids* **51**, 367–371 (2019).
16. J. Xu *et al*., Graded perturbations of metabolism in multiple regions of human brain in Alzheimer's disease: Snapshot of a pervasive metabolic disorder. *Biochim. Biophys. Acta* **1862**, 1084–1092 (2016).
17. R. Kaddurah-Daouk *et al*., Metabolomic changes in autopsy-confirmed Alzheimer's disease. *Alzheimers Dement.* **7**, 309–317 (2011).
18. M. Kori, B. Aydın, S. Unal, K. Y. Arga, D. Kazan, Metabolic biomarkers and neurodegeneration: A pathway enrichment analysis of Alzheimer's disease, Parkinson's disease, and amyotrophic lateral sclerosis. *OMICS* **20**, 645–661 (2016).
19. E. Trushina, M. M. Mielke, Recent advances in the application of metabolomics to Alzheimer's disease. *Biochim. Biophys. Acta* **1842**, 1232–1239 (2014).
20. M. S. Morris, Homocysteine and Alzheimer's disease. *Lancet Neurol.* **2**, 425–428 (2003).
21. F. Van Dam, W. A. Van Gool, Hyperhomocysteinemia and Alzheimer's disease: A systematic review. *Arch. Gerontol. Geriatr.* **48**, 425–430 (2009).
22. S. Seshadri *et al*., Plasma homocysteine as a risk factor for dementia and Alzheimer's disease. *N. Engl. J. Med.* **346**, 476–483 (2002).
23. R. M. Soni, S. C. Tiwari, A. A. Mahdi, N. Kohli, Serum homocysteine and behavioral and psychological symptoms of dementia: Is there any correlation in Alzheimer's disease? *Ann. Neurosci.* **25**, 152–159 (2019).
24. I. Sleeman *et al*., Urate and homocysteine: Predicting motor and cognitive changes in newly diagnosed Parkinson's disease. *J. Parkinsons Dis.* **9**, 351–359 (2019).
25. M. C. Bakeberg *et al*., Elevated serum homocysteine levels have differential gender-specific associations with motor and cognitive states in Parkinson's disease. *Parkinsons Dis.* **2019**, 3124295 (2019).
26. L. Baroni *et al*., Association between cognitive impairment and vitamin B12, folate, and homocysteine status in elderly adults: A retrospective study. *J. Alzheimers Dis.* **70**, 443–453 (2019).
27. T. den Heijer *et al*., Homocysteine and brain atrophy on MRI of non-demented elderly. *Brain* **126**, 170–175 (2003).
28. J. P. Kraus *et al*., Cystathionine β-synthase mutations in homocystinuria. *Hum. Mutat.* **13**, 362–375 (1999).
29. B. L. Zaric *et al*., Homocysteine and hyperhomocysteinaemia. *Curr. Med. Chem.* **26**, 2948–2961 (2019).
30. J. Kim, H. Kim, H. Roh, Y. Kwon, Causes of hyperhomocysteinemia and its pathological significance. *Arch. Pharm. Res.* **41**, 372–383 (2018).
31. J. Zou *et al*., Trefoil factor 3, cholinesterase and homocysteine: Potential predictors for Parkinson's disease dementia and vascular parkinsonism dementia in advanced stage. *Aging Dis.* **9**, 51–65 (2018).
32. N. Licking *et al*., Homocysteine and cognitive function in Parkinson's disease. *Parkinsonism Relat. Disord.* **44**, 1–5 (2017).
33. P. Saadat *et al*., Serum homocysteine level in Parkinson's disease and its association with duration, cardinal manifestation, and severity of disease. *Parkinsons Dis.* **2018**, 5813084 (2018).
34. A. D. Smith *et al*., Homocysteine and dementia: An international consensus statement. *J. Alzheimers Dis.* **62**, 561–570 (2018).
35. P. I. Ho, D. Ortiz, E. Rogers, T. B. Shea, Multiple aspects of homocysteine neurotoxicity: Glutamate excitotoxicity, kinase hyperactivation and DNA damage. *J. Neurosci. Res.* **70**, 694–702 (2002).
36. I. I. Kruman *et al*., Folic acid deficiency and homocysteine impair DNA repair in hippocampal neurons and sensitize them to amyloid toxicity in experimental models of Alzheimer's disease. *J. Neurosci.* **22**, 1752–1762 (2002).
37. P. Pierozan *et al*., Synergistic toxicity of the neurometabolites quinolinic acid and homocysteine in cortical neurons and astrocytes: Implications in Alzheimer's disease. *Neurotox. Res.* **34**, 147–163 (2018).
38. L. F. Agnati *et al*., Abeta peptides as one of the crucial volume transmission signals in the trophic units and their interactions with homocysteine. Physiological implications and relevance for Alzheimer's disease. *J. Neural Transm. (Vienna)* **114**, 21–31 (2007).
39. C. E. Zhang *et al*., Hyperhomocysteinemia increases β-amyloid by enhancing expression of γ-secretase and phosphorylation of amyloid precursor protein in rat brain. *Am. J. Pathol.* **174**, 1481–1491 (2009).
40. N. Shirafuji *et al*., Homocysteine increases tau phosphorylation, truncation and oligomerization. *Int. J. Mol. Sci.* **19**, 891 (2018).
41. L. Adler-Abramovich *et al*., Phenylalanine assembly into toxic fibrils suggests amyloid etiology in phenylketonuria. *Nat. Chem. Biol.* **8**, 701–706 (2012).
42. E. Gazit, Metabolite amyloids: A new paradigm for inborn error of metabolism disorders. *J. Inherit. Metab. Dis.* **39**, 483–488 (2016).
43. S. Shaham-Niv, L. Adler-Abramovich, L. Schnaider, E. Gazit, Extension of the generic amyloid hypothesis to nonproteinaceous metabolite assemblies. *Sci. Adv.* **1**, e1500137 (2015).
44. S. Shaham-Niv *et al*., Formation of apoptosis-inducing amyloid fibrils by tryptophan. *Isr. J. Chem.* **57**, 729–737 (2017).
45. O. Tavassoly *et al*., Quinolinic acid amyloid-like fibrillar assemblies seed α-synuclein aggregation. *J. Mol. Biol.* **430**, 3847–3862 (2018).
46. B. G. Anand, K. Dubey, D. S. Shekhawat, K. Kar, Intrinsic property of phenylalanine to trigger protein aggregation and hemolysis has a direct relevance to phenylketonuria. *Sci. Rep.* **7**, 11146 (2017).
47. D. Sade, S. Shaham-Niv, Z. A. Arnon, O. Tavassoly, E. Gazit, Seeding of proteins into amyloid structures by metabolite assemblies may clarify certain unexplained epidemiological associations. *Open Biol.* **8**, 170229 (2018).
48. D. Laor *et al*., Fibril formation and therapeutic targeting of amyloid-like structures in a yeast model of adenine accumulation. *Nat. Commun.* **10**, 62 (2019).
49. S. Rencus-Lazar, Y. DeRowe, H. Adsi, E. Gazit, D. Laor, Yeast models for the study of amyloid-associated disorders and development of future therapy. *Front. Mol. Biosci.* **6**, 15 (2019).
50. S. Shaham-Niv *et al*., Differential inhibition of metabolite amyloid formation by generic fibrillation-modifying polyphenols. *Commun. Chem.* **1**, 1–11 (2018).
51. P. A. Williams, C. E. Hughes, K. D. M. Harris, L-lysine: Exploiting powder X-ray diffraction to complete the set of crystal structures of the 20 directly encoded proteinogenic amino acids. *Angew. Chem. Int. Ed. Engl.* **54**, 3973–3977 (2015).

52. C. H. Görbitz, K. Vestli, R. Orlando, A solution to the observed $Z' = 2$ preference in the crystal structures of hydrophobic amino acids. *Acta Crystallogr. B* **65**, 393–400 (2009).
53. C. H. Görbitz, Crystal structures of amino acids: From bond lengths in glycine to metal complexes and high-pressure polymorphs. *Crystallogr. Rev.* **21**, 160–212 (2015).
54. S. Bera, S. Mondal, S. Rencus-Lazar, E. Gazit, Organization of amino acids into layered supramolecular secondary structures. *Acc. Chem. Res.* **51**, 2187–2197 (2018).
55. T. D. Do, W. M. Kincannon, M. T. Bowers, Phenylalanine oligomers and fibrils: The mechanism of assembly and the importance of tetramers and counterions. *J. Am. Chem. Soc.* **137**, 10080–10083 (2015).
56. C. Bleiholder, N. F. Dupuis, T. Wyttenbach, M. T. Bowers, Ion mobility-mass spectrometry reveals a conformational conversion from random assembly to β-sheet in amyloid fibril formation. *Nat. Chem.* **3**, 172–177 (2011).
57. T. D. Do *et al*., Amino acid metaclusters: Implications of growth trends on peptide self-assembly and structure. *Anal. Chem.* **88**, 868–876 (2016).
58. S. Shaham-Niv *et al*., Intrinsic fluorescence of metabolite amyloids allows label-free monitoring of their formation and dynamics in live cells. *Angew. Chem. Int. Ed. Engl.* **57**, 12444–12447 (2018).
59. A. Šarić, T. C. T. Michaels, A. Zaccone, T. P. J. Knowles, D. Frenkel, Kinetics of spontaneous filament nucleation via oligomers: Insights from theory and simulation. *J. Chem. Phys.* **145**, 211926 (2016).
60. W. Hwang, S. Zhang, R. D. Kamm, M. Karplus, Kinetic control of dimer structure formation in amyloid fibrillogenesis. *Proc. Natl. Acad. Sci. U.S.A.* **101**, 12916–12921 (2004).
61. A. R. White *et al*., Homocysteine potentiates copper- and amyloid beta peptide-mediated toxicity in primary neuronal cultures: Possible risk factors in the Alzheimer's-type neurodegenerative pathways. *J. Neurochem.* **76**, 1509–1520 (2001).
62. B. Ono *et al*., Cysteine biosynthesis in *Saccharomyces cerevisiae*: Mutation that confers cystathionine beta-synthase deficiency. *J. Bacteriol.* **170**, 5883–5889 (1988).
63. E. M. Weekman, A. E. Woolums, T. L. Sudduth, D. M. Wilcock, Hyperhomocysteinemia-induced gene expression changes in the cell types of the brain. *ASN Neuro* **9**, 1759091417742296 (2017).
64. J. Guo, S. Ni, Q. Li, J. Z. Wang, Y. Yang, Folate/Vitamin B alleviates hyperhomocysteinemia-induced Alzheimer-like pathologies in rat retina. *Neurosci. Bull.* **35**, 325–335 (2019).
65. H. Oakley *et al*., Intraneuronal β-amyloid aggregates, neurodegeneration, and neuron loss in transgenic mice with five familial Alzheimer's disease mutations: Potential factors in amyloid plaque formation. *J. Neurosci.* **26**, 10129–10140 (2006).
66. S. Kalinin, J. C. Richardson, D. L. Feinstein, A PPARdelta agonist reduces amyloid burden and brain inflammation in a transgenic mouse model of Alzheimer's disease. *Curr. Alzheimer Res.* **6**, 431–437 (2009).
67. R. Diaz-Arrastia, Homocysteine and neurologic disease. *Arch. Neurol.* **57**, 1422–1427 (2000).
68. Y. H. Chung, K. M. Joo, Y. J. Lee, C. I. Cha, Immunohistochemical study on the distribution of MnSOD in the central nervous system of the transgenic mice expressing a human Cu/Zn SOD mutation. *Brain Res.* **990**, 215–220 (2003).
69. D. Braconi *et al*., Homogentisic acid induces aggregation and fibrillation of amyloidogenic proteins. *Biochim. Biophys. Acta Gen. Subj.* **1861**, 135–146 (2017).
70. G. C. Román, O. Mancera-Páez, C. Bernal, Epigenetic factors in late-onset Alzheimer's disease: *MTHFR* and *CTH* gene polymorphisms, metabolic transsulfuration and methylation pathways, and B vitamins. *Int. J. Mol. Sci.* **20**, 319 (2019).
71. S. Ibrahim, S. Maqbool, M. Azam, M. P. Iqbal, R. Qamar, CBS mutations and MTFHR SNPs causative of hyperhomocysteinemia in Pakistani children. *Mol. Biol. Rep.* **45**, 353–360 (2018).
72. M. T. Mursleen, S. Riaz, Implication of homocysteine in diabetes and impact of folate and vitamin B12 in diabetic population. *Diabetes Metab. Syndr.* **11**, S141–S146 (2017).
73. G. J. Hankey, J. W. Eikelboom, Homocysteine and vascular disease. *Lancet* **354**, 407–413 (1999).
74. A. Pinna, F. Zaccheddu, F. Boscia, C. Carru, G. Solinas, Homocysteine and risk of age-related macular degeneration: A systematic review and meta-analysis. *Acta Ophthalmol.* **96**, e269–e276 (2018).
75. D. Zhang, X. Wen, W. Wu, Y. Guo, W. Cui, Elevated homocysteine level and folate deficiency associated with increased overall risk of carcinogenesis: Meta-analysis of 83 case-control studies involving 35,758 individuals. *PLoS One* **10**, e0123423 (2015).
76. R. Martínez-Vega *et al*., Folic acid deficiency induces premature hearing loss through mechanisms involving cochlear oxidative stress and impairment of homocysteine metabolism. *FASEB J.* **29**, 418–432 (2015).
77. A. Altomare *et al*., EXPO2013 : A kit of tools for phasing crystal structures from powder data. *J. Appl. Cryst.* **46**, 1231–1235 (2013).
78. B. H. Toby, R. B. Von Dreele, GSAS-II: The genesis of a modern open-source all purpose crystallography software package. *J. Appl. Cryst.* **46**, 544–549 (2013).